

Developing Novel Contrast-to-Noise Ratio Thresholds for the Detection of MCF-7 Breast Cancer Tissue in Acoustic Shadows

Hari Desikan

Mentors: Dr. Jonathan Bennett, Mr. Ben Levy

Abstract

Recent findings show that metastasizing cancer cell clusters form in the primary tumor rather than at the site of metastasis, allowing them to be identified before metastasis occurs. I investigated the extent to which shadows cast by MCF-7 breast cancer tissue phantoms disrupted the detectability of posterior MCF-7 tissue. Using an Ultrasonix L14-5/38 linear array ultrasound transducer, my mentor imaged a 29.5 mm x 38.0 mm tissue phantom with a square lesion of side length 10 mm and attenuation 1.56 dB/cm/MHz. Analyzing resultant data, I determined parameters including the enveloped radiofrequency data corresponding to the acoustic shadowing effect. I then matched these parameters in simulations. I then used Field II to simulate a Shadow Caster (SC) region of MCF-7 tissue casting a shadow on a Region of Detection (RoD). The contrast-to-noise ratio (CNR) metric was used to contrast the detectability of the RoD when it did and did not contain MCF-7 tissue. The relationship between the CNR of the RoD and the position and axial dimension of the SC region was documented. I found that the CNR of shadowed MCF-7 tissue regions is higher than the CNR of shadowed healthy regions. Relationships determined between the CNR and geometric properties of simulations are used to compute CNR thresholds such that shadowed regions with CNR greater than corresponding thresholds are considered to likely contain abnormal tissue. My results have the possibility to be used to identify cancerous regions within acoustic shadows in clinical settings.

1 Introduction

1.1 Bone Metastasis

Breast cancer is the leading cause of cancer and the second most common cause of cancer death in females. Quickly diagnosing and treating breast cancers is a major concern [13]. Bone metastasis is the process by which cancer cells escape a tumor, travel through the bloodstream, and land ready to colonize a distant site. The most common such sites are the spine, ribs, and pelvis. Autopsy studies have reported bone metastases in 47 to 85% of women dying of breast cancer. The median survival rate for those with detected bone metastasis is 2 years past diagnosis. [6]. It is estimated that 90% of cancer-related deaths are related to metastasis [12]. Older models of bone metastasis postulated that many single breast cancer cells would enter the bloodstream and very few would survive the journey to a distant bone to then clone at and colonize the bone. Clinical observations of cell clusters in the bloodstream have not supported these models and recent studies [3] instead suggest that metastatic cancer cells clone before entering the bloodstream. This has implications on the prognosis of the cancer at the new organ. Advances in identifying cells that are expected to become involved with metastasis imply that cells with the K14⁺ protein are highly likely to metastasize [3]. Since metastasis is now attributed to cell clusters, metastasizing cell clusters show up on images created by various imaging systems [2]. Ultrasound imaging systems are the natural choice to identify these cells before they reach their target because ultrasound is already often used to differentiate between benign and malignant tumors owing to its relatively low associated costs [1] and high degree of accuracy [18]. Additionally, early-stage treatments of breast cancer tumors incorporating high-frequency ultrasound have been developed as a low-cost, noninvasive alternative to x-ray therapy [5]. Transitioning fully from x-ray technology to ultrasound technology for the treatment of breast cancers will lead to a large decrease in start-up costs for hospitals specializing in cancer treatment.

1.2 Acoustic Shadowing

Ultrasound waves permeate tissue relatively unimpeded and so are often used to image subsurface tissue [16]. Breast cancer tissue attenuates ultrasound waves much more than non-cancerous tissue [15] [8] , resulting in dark acoustic shadow regions beyond the part of a cancerous tumor closest to the transducer. This shadow region can hide regions of breast cancer from clinicians observing ultrasound images. A common theme with the levels of shadowing generated from breast cancer tissues is that a region of cancerous tissue may shadow parts of the same tissue unit further away from the transducer. The prognosis of metastatic cancer is very sensitive to the size of the metastasizing cell cluster [6], and knowing the precise size and location of the cluster is relevant to all forms of treatment.

1.3 Outline of Application

When a patient is checked for breast cancer, clinicians first search ultrasound images for abnormalities. (Regions of acoustic shadow by themselves are not considered abnormal, as breast cancers are highly attenuating.) Images are then analyzed by a computer [17].

Breast cancer regions in acoustic shadows are unlikely to be identified as such by either of these means. The contrast-to-noise ratio (CNR) of a particular region R of a b-mode image is defined as

$$CNR = \frac{S_{in} - S_{out}}{\sigma_{out}},$$

where S_{in} is the mean signal in R (henceforth “in-region”), S_{out} is the mean signal in a region R' (henceforth “out-region”) close to R , and σ_{out} is the standard deviation of the signal in R' [14]. A region with negative CNR is darker than its surroundings. The CNR quantifies the detectability to the naked human eye of a particular region of tissue in an ultrasound image (at least, one that has not been processed nonlinearly [11]). A region with $CNR > 1$ is considered to be visible [9]. As will soon be evident, regions in acoustic shadows cast by breast cancer tissue often have CNR values lower than 1 - we thus use the CNR to distinguish between the contrast of various regions that all appear undetectable to the naked human eye.

The natural course of action is to determine a separate CNR threshold value (TCNR) for regions in acoustic shadows cast by breast cancer tissue such that I can confidently claim a shadowed region with $CNR > TCNR$ hosts additional breast cancer tissue. This threshold is specific to abnormalities with attenuation similar to that of MCF-7 breast cancer tissue.

A cancerous region directly in the shadow of another will have a lower CNR than the same cancerous region only partially in the shadow of another, and so the TCNR for the first case should be lower to compensate. Additionally, ultrasound waves approaching a cancerous region after being attenuated by a long cancerous region will be weaker than if the shadowing region is shorter. The TCNR for this case should also be lower to compensate for this effect. The TCNR thus depends on the relative locations of the tissue casting the shadow, or the “Shadow Caster” (SC) region, and the cancerous “Target Region” (TR) hidden in the acoustic shadow cast by the SC.

I outline an additional quantitative test for patients known to harbor breast cancer tumors predicted to metastasize: determine the CNRs of many subregions of shadowed regions. If any of these subregions (henceforth “regions of detection” (RoD)) have CNR exceeding the TCNR for the specific RoD, breast cancer tissue is present in the RoD. (The distinction between the TR and the RoD is subtle: the RoD is a region surveyed for the existence of cancerous tissue where it might not exist, while the TR specifically refers to the cancerous tissue present in that region when it is assumed that cancerous tissue is present in the RoD.)

This paper focuses on determining the TCNR as a function of both the length of the SC through which waves are attenuated and the relative positions of the SC and RoD. This is done by moving the SC and measuring the CNR of a fixed RoD that sometimes hosts a TR. Clinically, the position of the SC would be fixed and the RoD would be moved around, but it is easier to simulate the

situation the other way around. The important quantity is the relative position between the SC and the RoD, and varying the position of the SC still varies this quantity.

2 Overview and Preliminary Experiments

2.1 Preliminary Conventions and Definitions

2.1.1 Wet Lab and dry Lab

A portion of the experiment took place in a lab at the University of North Carolina at Chapel Hill (UNC). I determined the specifications for a tissue phantom, and Ben Levy (a listed mentor) created and imaged the phantoms because expensive equipment was involved. This portion of the experiment is not computational in nature, and I refer to it as the “wet lab” or similarly. To contrast, the “dry lab” portions of the experiment are exclusively computational and carried out by me in MATLAB.

2.1.2 Brightness Mode Image

Ultrasound images are displayed on a brightness-mode: brighter regions in an image roughly correspond to regions that reflected more waves back to the transducer. For this reason, they are called b-mode images.

2.1.3 Axial and Lateral Directions

Any time dimensions of a region are specified, the axial dimension (how long a region is in the axial direction) is specified before the lateral dimension (defined similarly). The axial direction is the average direction ultrasonic waves propagate in, while the lateral direction is perpendicular to the axial direction. Both of these directions lie in the plane of the produced image. In b-mode images, the axial direction is vertical and increases downward while the lateral direction is horizontal and increases rightward. The ultrasound transducer is always positioned directly above the b-mode image, out of the imaging area. Artifacts near the top of an ultrasound image are reflections from the ultrasound impedance matching layer used, not b-mode images of the transducer.

2.1.4 Radiofrequency (RF) Data

An ultrasound transducer, upon imaging a region of tissue returns a matrix of radiofrequency (RF) data. These values are noisy and vary sinusoidally, so they must be processed before they are plotted. The most important part of processing this data is enveloping it, which results in enveloped radiofrequency data (ENV data.) Plotting ENV data on a brightness mode results in the b-mode images described previously.

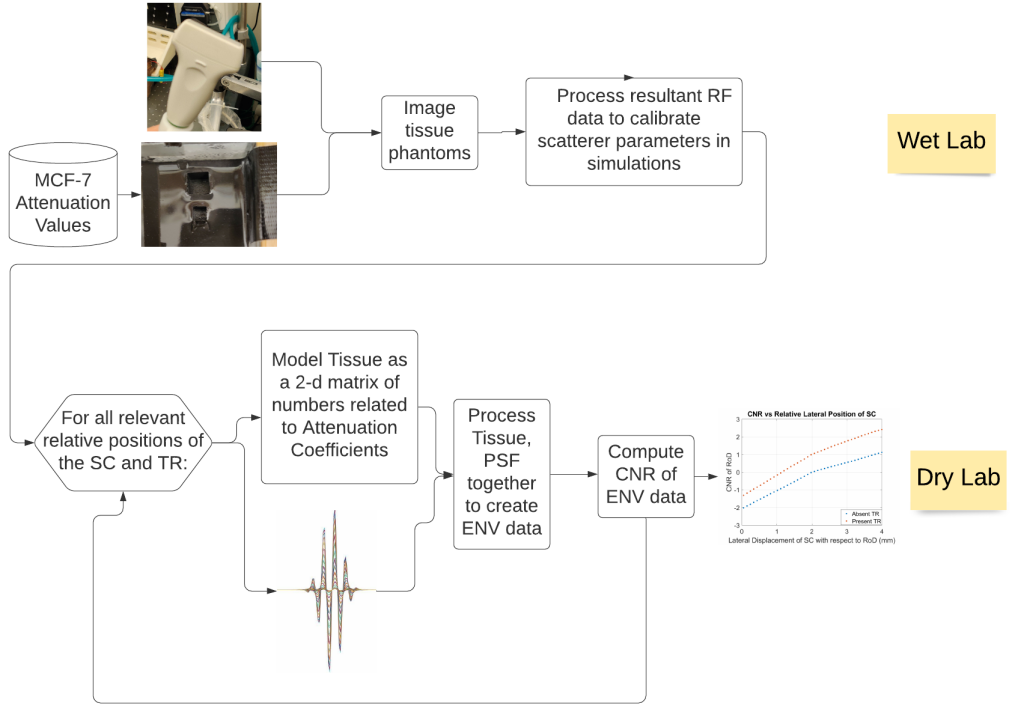


Figure 1: A general procedure to be followed, following the paper as far as data collection

2.2 Justification of Computational Ultrasound Methods

The experiment to be detailed is meant to compare quantitative characteristics of a large number of geometrically-distinct configurations of tissue. It is not feasible to physically create all such configurations. It took around 8 hours for my mentor to create and image the tissue phantoms used to create a single calibration image; my experiment considers 3948 such images created 10 times each. The materials used to create the phantoms were also fairly expensive. I thus turned to computational methods. A large concern for simulated ultrasound experiments is the preservation of speckle — the small-scale fluctuation in how a b-mode image appears due to small-scale interactions of ultrasound waves with small tissue cells. The Field II software for MATLAB models the speckle quite well, and so was chosen for the simulation.

Figure 1 displays an outline of our procedures to explain how observations from the wet lab will be used to calibrate parameters of the dry lab.

3 Calibration Experiment

3.1 Outline of Procedure

The first step in simulating the effects of shadows cast by breast cancer tissue is to determine both the degree to which shadowing occurs and the natural brightness of breast cancer tissue in b-mode images. If breast cancer tissue appears very bright in clinical images, for example, it is

possible the shadowing effect is comparatively not powerful enough to significantly decrease the visibility of tissue.

A variety of data is present on the MCF-7 breast cancer line, and so we survey phantoms of this particular breast cancer. It is known that the MCF-7 breast cancer line has acoustic attenuation $\alpha = 1.56 \text{ dB/cm/MHz}$ [15] and that healthy human tissue has acoustic attenuation 0.3 dB/cm/MHz [8]. Field II only allows for the background attenuation to be specified. Additionally, we cannot simply “code in” a signal loss of 1.56 dB/cm/MHz in the SC region because the specified attenuation is not that of the ENV data but that of ultrasound waves. The fundamental difficulty here is conversion between ENV data and values in the literature. Field II allows us to specify “Brightness Coefficients” (BCs) for our data, but these are just a proxy for the resultant ENV data produced in the simulated image. The software lets us specify the data values it will output instead of the physical values that go into creating such data. Pham *et al.* have documented some loosely related conversion values [10], but they are very general and are not sufficient for my purposes. For this reason, I chose instead to image phantoms tissue in a wet lab. The planned procedure was to extract the ENV values present in the resulting wet lab (calibration) image where the cancerous tissue was and to use them to specify BC values for further simulations in Field II.

Field II lacks the ability to produce the true acoustic shadowing effect due to software limitations, so the characteristics of the acoustic shadows of cancer-cell clusters I seek must also be observed in the calibration image so they can be modelled in dry lab simulations.

3.2 Wet Lab Parameters

We include for purposes of replication the parameters used for simulation. We used an Ultrasonix L14-5/38 linear array transducer centered at 7.2 MHz at an elevation of 4 mm at an imaging frequency of 10 MHz with elements having a width of 0.2798 mm, a pitch of 0.3048 mm, a kerf-value of 0.025 mm, a fractional bandwidth of 70%, and focused 25.0 mm axially from its center. The imaging area has dimensions 29.5 mm x 38.0 mm and is a cross-sectional subregion of a much larger surrounding region. The transducer is shown in Figure 2.



Figure 2: The Ultrasonix L14-5/38 linear array transducer used in the calibration experiment

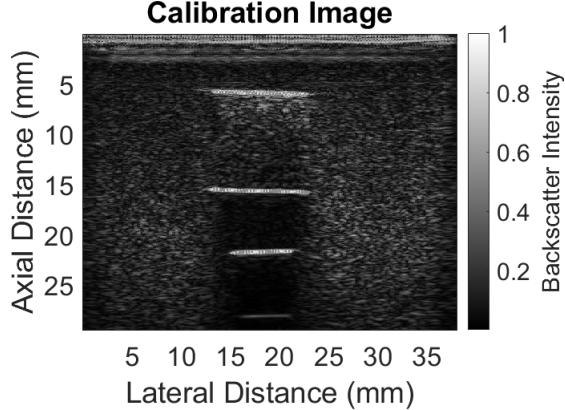


Figure 3: Calibration image (wet lab)

The imaging area contains an SC square lesion of side-length 10.0 mm centered 110 mm axially and 180 mm laterally, and a directly posterior “Target Region” TR square lesion of side-length 6.30 mm centered 250 mm axially and 180 mm laterally. These regions of tissue phantoms have acoustic attenuation similar to those of MCF-7 breast cancer tissue, while the surrounding background tissue phantoms have acoustic attenuation similar to that of normal human tissue. This geometry of scatterers is henceforth referred to as (G). The produced image is shown in Figure 3.

To create tissue phantoms of varying attenuation, I sent acoustic attenuation values to Ben Levy, who used a procedure detailed in Madsen *et al.* [7] and sent me the resulting data. The TR and SC lesions were created to have acoustic attenuation $\alpha = 1.56 \text{ dB/cm/MHz}$ to match the acoustic attenuation of MCF-7 cancer cells [15], and the background has acoustic attenuation 0.3 dB/cm/MHz to match the commonly accepted acoustic attenuation of human tissue [8]. The graphite concentrations my mentor used to create the phantoms were the most important in determining acoustic attenuation values [7], and so are displayed in Table 1.

Table 1: Acoustic attenuations vs graphite concentrations used in solution

	Graphite Concentration (g/mL)	Acoustic Attenuation (dB/cm/MHz)
Background Speckle	0.048	0.3
MCF-7 Phantom	0.236	1.56

3.3 Limitations of Calibration Data

The bright lines present in the data here correspond to boundaries between regions of differing concentrations of gelatin, graphite, and n-propanol. They are not seen in clinical b-mode images. The reason for these artifacts is not yet understood. Whatever the case may be, the acoustic shadowing data that I use for calibration extends from the uppermost bright white line to the second white line from the top of the image. For all dry lab purposes, I omit the data present at the locations of these white lines because they are not observed in clinical images. This limitation

gives me 10 mm of data in the axial direction to calibrate the ENV data in acoustic shadows; in the dry lab, the entire RoD must always fall within these 10 mm.

3.4 Calibration

(G) was imaged by the transducer. The resultant RF data was enveloped. The ENV data was recorded in 3 regions: (A), a region with axial bounds 15 mm - 20 mm and lateral bounds 27 mm - 32 mm, far from any shadowing effects to provide a baseline for the RF data corresponding to regions of background speckle; (B) a region with axial bounds 6.3 mm - 7.5 mm and lateral bounds 17.5 mm - 18.5 mm, where the MCF-7 phantom is present and not expected to be significantly shadowed to calibrate the natural brightness of the MCF-7 regions; and (C) a region with axial bounds 8 mm - 15 mm and lateral bounds 16 mm - 20 mm with high attenuation to calibrate the effects of acoustic shadows. The three regions are outlined in Figure 4.

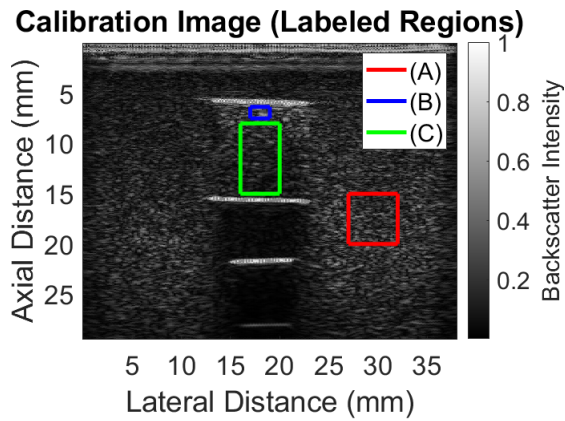


Figure 4: Three regions used for calibration

I then simulated a linear-array transducer in Field II with parameters similar to those present in the physical L14-5/38 transducer: an imaging frequency of 10 MHz, a pitch of 0.3048 mm, a kerf-value of 0.025 mm, a fractional bandwidth of 70%, and focused 25.0 mm axially from its center. This is also, incidentally, the same transducer used for all dry lab components of this paper.

To simulate scatterer geometries in MATLAB, I used a technique specified in Jørgen Arendt Jensen *et al.* 1997 [4]; as a 2d matrix of values corresponding to a 2d collection of discrete “scatterers” with varying BCs. Scatterers are models of cells scattering acoustic waves, with the entries in the matrix being related to the ENV data that will be produced by the particular region corresponding to the entry.

I simulated a 30.0 mm x 30.0 m square imaging area to optimize the accuracy of mathematical functions used by Field II. The imaging area contains an SC square lesion of side-length 10.0 mm centered 10.0 mm axially and 15.0 mm laterally. No TR was simulated to emphasize that no data from that region of the calibration image was used for calibration. The bounds of regions (A), (B), and (C) in simulated images were adjusted to account for the adjustment of the dimensions of the imaging area. In simulated images used for calibration, (A) has axial bounds 15.0 mm - 20.0 mm

and lateral bounds 22.0 mm - 27.0 mm; (B) has axial bounds 6.0 mm - 7.0 mm and lateral bounds 14.5 mm - 15.5 mm; and (C) has axial bounds 8.0 mm - 15.0 mm and lateral bounds 13.0 mm - 17.0 mm

First, I sought to calibrate the natural (before shadowing) brightness of the SC and TR regions with respect to the background tissue. To do so, I computed the ratio between the average ENV data in (B) and the average ENV data in (A) in the calibration image. The computed ratio was 1.4610. I then tuned the parameter corresponding to the relative brightness of regions modelling MCF-7 tissue in a dry lab image to match the observed (B):(A) ratio. I did this by iteratively changed the BCs of the SC region in Field-II, starting at BC = 1.4 and ending at BC = 1.5 with a stepsize of $\Delta BC = .005$, recording the corresponding (B):(A) ENV ratio in the average of 10 simulated b-mode images corresponding to any particular BC. Figure 5 shows the relationship between (B):(A) ENV ratios and BC values. BCs of 1.463 and 1.468 resulted in (B):(A) ENV ratios near 1.4610, and linearizing the plot between those two points suggests that setting the BC of the SC to $BC = 1.47 \pm .01$ best models the data present in the calibration image. I henceforth use a BC of 1.47 for the SC (and eventually, the TR) in all further simulations. Figure 6 shows an example of using this BC value to simulate (A) and (B).

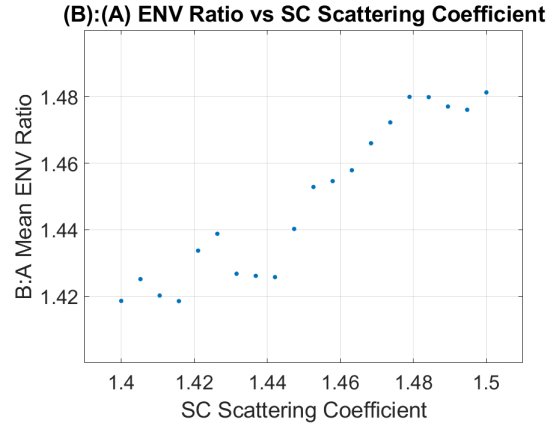


Figure 5: The (B):(A) ENV ratios are recorded for a variety of BCs. It turns out that BCs do a good job at specifying ENV ratios.

3.4.1 Acoustic Shadow Model

My model of acoustic shadows is as follows: I take (C) in the calibration image and in the dry lab image (with dimensions 7 mm x 4 mm in both images) and partition it into 7 subregions (C_1, C_2, \dots, C_7) (with subscripts increasing with axial distance) of dimensions 1 mm x 4 mm. For each subregions in the calibration image, I tune the corresponding BC in the dry lab image such that the ENV data in C_i in the calibration image matches the ENV data for each C_i . The 7 subregions of (C) in the calibration image are shown in Figure 7.

My results calibrate a model of the acoustic shadow as it affects regions of MCF-7 tissue phantoms (as (C) is entirely composed of MCF-7 tissue phantoms). In future simulations, segments

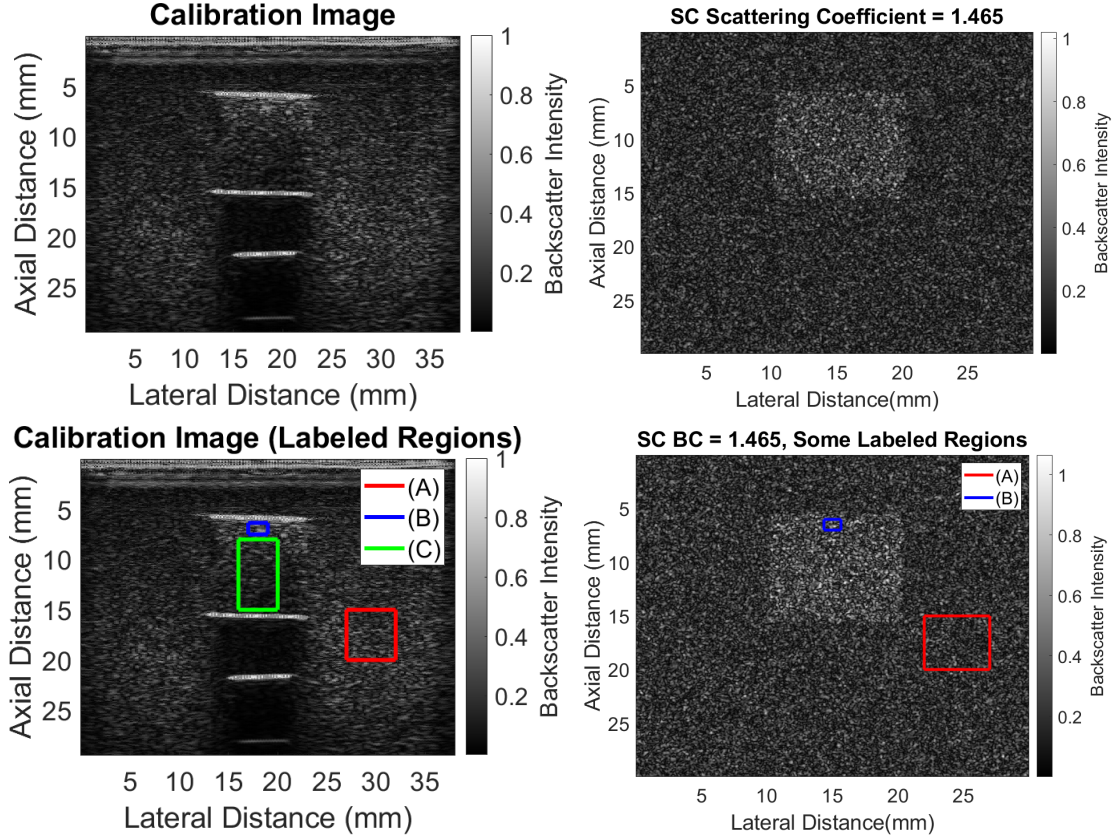


Figure 6: The calibration images with and without labelled regions are shown side-by-side with corresponding simulated b-mode images that match the (B):(A) ENV ratio. Note that (A) and (B) in the calibration image have dimensions similar to (A) and (B) in the simulated image. (C) corresponds to the shadow region and has not thus been calibrated, and is thus not outlined in the simulated image. The white-line artifacts are not present in the dry lab image.

of the shadow will also fall upon regions of healthy tissue. For these cases, I extrapolate that the effect of a particular portion of an acoustic shadow on an arbitrary region of tissue is to multiply BCs in the region of tissue by some constant factor. For example, the shadow will multiply BCs in (C_1) by one value, all BCs in (C_2) by another, and so on, independent of the natural brightnesses of the regions to which it is applied. These (7) values will henceforth be called “shadow parameters” (SPs) and will be computed for each C_i as follows:

$$SP_i = \frac{BC_i}{BC'_i},$$

where BC_i is the computed BC for the region C_i and BC'_i is what the BC in region C_i would be if there was no shadowing. $BC'_i = 1.47$ for all i , as was measured in the calibration image. This allows my shadow model to decrease the visibility of regions of healthy tissue as observed in real images. I computed the ratios of the average ENV data for each (C_i) and in (A). I then computed the BC value for each C_i that will result in a matching ENV ratio in simulated images, simulating

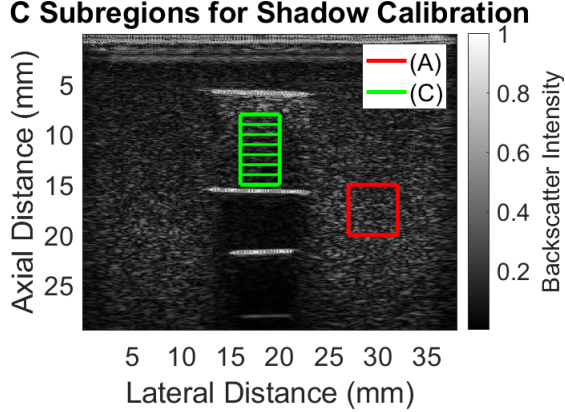


Figure 7: C_1, C_2, \dots, C_7 are shown, outlined in green. C_1 is the region closest to the transducer (the uppermost region). (C) only begins after 3 mm of shadowing region — before that point, the effective brightness is considered unaltered for simplicity of separating (B) and (C).

and averaging 10 images for every BC value before computing the BC value as was done for region (B). I compute the ratio between the calculated BC value and the natural BC value (1.47) for each subregion - this will be the factor by which I multiply BCs in regions that are supposed to be shadowed to introduce the shadowing effect in future simulations. Results are displayed in Table 2.

Table 2: Observed mean ENV ratios, computed brightness coefficients, and computed shadowing parameters are displayed for all 7 subregions of C.

i	1	2	3	4	5	6	7
$\frac{\overline{ENV}_{C_i}}{\overline{ENV}_A}$	0.9416	0.8336	0.6978	0.6723	0.6206	0.5409	0.5217
BC_i	0.94	0.84	0.69	0.67	0.62	0.54	0.52
$SP_i (= \frac{BC_i}{1.47})$	0.64	0.57	0.47	0.46	0.42	0.37	0.35

It should be noted that the BC of a region roughly specifies the ratio between the ENV data in that region and the ENV data in a distant, baseline region in the dry lab image.

Using the determined SP_i values, I simulated an ultrasound image with acoustic shadows in (C) matching ENV values from the calibration image. The image also matches the (B):(A) ENV ratio measured in the calibration image and is shown in Figure 8.

4 Methods and Results

I now seek to simulate an SC with the previously calibrated trailing shadow and an RoD potentially containing a TR, keeping the RoD in place and moving the SC. Since I only have 10

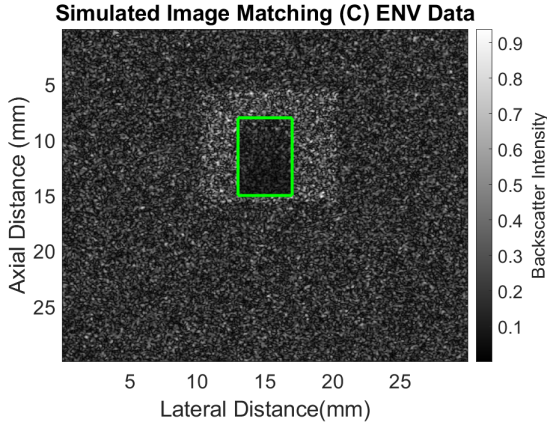


Figure 8: A simulated image matching ENV data from (A), (B), and (C). The shadow effect is clearly visible in (C), and was not applied outside of (C). (C) is outlined in green.

mm of data calibrating the acoustic shadowing effect, I choose the RoD to be a square region of side-length 4mm. This allows for the RoD to fall completely within the shadow of the SC for a variety of dimensions and positions of the SC.

Recall that my experiments vary the position of the SC and not the RoD, even though in clinical settings the position of the SC is known and the RoD will be varied. For each experiment, the RoD is held in place as a square region centered at 25 mm axially and 15 mm laterally with sidelength 4 mm. This region is the in-region used for CNR calculations. The focus of the transducer is incident with the center of the RoD. When the TR is present, it is located in the RoD with the same dimensions and position as the RoD. In all simulations, the relationship between the CNR of the RoD with the location of the SC will be measured.

In changing the relative lateral position of the SC and the RoD or the axial dimension of the SC, a few of the SCs parameters remain constant. The SC is modelled as a rectangular region of tissue with lateral dimension 4 mm. (In Experiment 1 and parts of Experiment 3, it is modelled as a square region.) The SC extends from a possibly varying initial axial position to an axial position of 22.7 mm. This ending axial position is 0.3 mm from the upper axial bound of the RoD. The SC casts a shadow 10.0 mm in the axial direction as calibrated in the calibration image. I measure the CNR of the RoD as different portions of it are placed in the shadow of the SC.

As a precursor to the bulk-image experiments, I first simulate three images to develop an idea of how CNR values differ between shadowed regions based on whether or not the regions host MCF-7 tissue. Figure 9 shows the result when the SC and RoD are laterally aligned and when the SC is a square region of side length 4 mm in each of three cases: 1) The shadows are absent and the TR is present, 2) The shadows are present and the TR is absent, and 3) The shadows are present and the TR is present. The magenta and yellow regions are the “in” and “out” regions, respectively, used to compute the CNR. (The out region used for calculations is the result when the two yellow regions are combined, resulting in an out-region with the same dimensions as the in-region.)

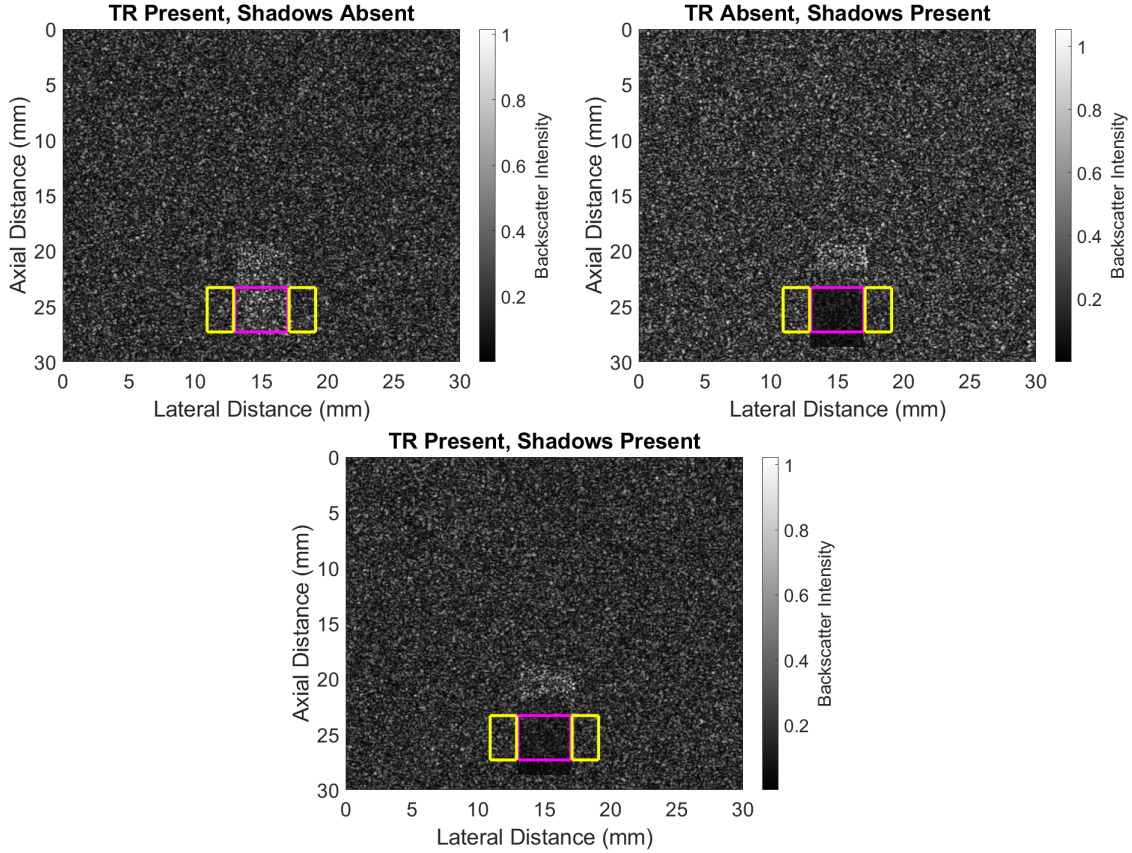


Figure 9: Examples of images with very different corresponding CNR values. Magenta outlines the “in-regions” and yellow outlines the “out-regions” used for CNR calculations. The RoD in the upper left image is visible; it has a CNR of 1.47. The RoD in the upper right image is distinctly darker from its surroundings; it has a CNR of -2.10. The RoD in the lower image is not quite visible, but speckle is somewhat brighter than in the upper-right image; it has a CNR of -1.40. In future images, I omit outlines of the in and out regions used to compute CNR values for image clarity.

4.1 Variation of CNR with Relative Lateral Positions of SC and RoD

Experiment 1 required approximately 5 minutes to simulate per run. All reported CNR values are average measured CNR values over 10 runs. In this experiment, the SC is a square region of side-length 4mm, axially centered about 20.7 mm. The lateral bounds of the SC are varied as detailed in Table 3.

Initial Axial Bounds (mm)	18.7 - 22.7
Initial Lateral Bounds (mm)	13.0 - 17.0
Final Axial Bounds (mm)	18.7 - 22.7
Final Lateral Bounds (mm)	9.0 - 13.0

Table 3: The Bounds of the SC in Experiment 1

The movement of the SC occurs in step-sizes of 0.1 mm to the left. ($\frac{1.5-1.1}{.01} + 1 = 41$ trials are expected — rounding effects due to conversion factors increment this count by 1.) Results are displayed in Figure 10. Examples of b-mode images corresponding to the first and last data points in Figure 10 in the cases of an absent TR and a present TR are shown in Figure 11.

Note that CNR values in the Absent TR plot rise to 1 when the shadow obscures the out region, making the RoD look brighter by comparison.

4.2 Variation of CNR with Relative Axial Positions of SC and RoD

Experiment 2 required approximately 6 minutes to simulate per run. All reported CNR values are average measured CNR values over 10 runs. In this experiment, the SC is a rectangular region, laterally centered about 15.0 mm. The SC is extended axially as detailed in Table 4:

Initial Axial Bounds (mm)	22.0 - 22.7
Initial Lateral Bounds (mm)	13.0 - 17.0
Final Axial Bounds (mm)	17.5 - 22.7
Final Lateral Bounds (mm)	13.0 - 17.0

Table 4: The Bounds of the SC in Experiment 2

The axial extension of the SC occurs in step-sizes of 0.1 mm upwards. The SC is always laterally centered above the RoD. My results are displayed in Figure 12. Examples of b-mode images corresponding to the first and last data points in Figure 12 in the cases of an absent TR and a present TR are shown in Figure 13.

4.3 2-Dimensional Relationship Between Relative Positions of SC and RoD and the CNR of the RoD

Experiment 3 required approximately 60 minutes to simulate per run. All reported CNR values are average measured CNR values over 10 runs.

In this experiment, the SC is both moved in the lateral dimension and extended in the axial direction. The lateral bounds of the SC are varied and the axial length of the SC is extended as detailed in Table 5.

Initial Axial Bounds (mm)	22.0 - 22.7
Initial Lateral Bounds (mm)	13.0 - 17.0
Final Axial Bounds (mm)	17.5 - 22.7
Final Lateral Bounds (mm)	9.0 - 13.0

Table 5: The Bounds of the SC in Experiment 3

The movement of the SC occurs in step-sizes of 0.2 mm to the left and extensions of the SC occur in step-sizes of 0.2 mm upwards.

This experiment details the how the CNR of the RoD changes as the SC is moved in two dimensions. My results are displayed in Figure 14. At a glance, the same, previously observed patterns persist: the CNR increases with the lateral displacement of the SC and decreases with the axial dimension of the SC. However, note that at high lateral displacements the CNR increases with the axial dimension of the SC! Although more axial extension equates to more shadowing, increased shadowing on regions near but not overlapping with the RoD increase its visibility by comparatively reducing the visibility of its surroundings.

4.4 Models

It should be noted that models developed here can only be used for interpolation and not extrapolation. If I extended data from Figure 10 any further, the line would slightly dip and then flatten out. This is because when the SC is laterally distant from the RoD, the shadowing effect is negligible. I am unable to extend Figure 12 more than 0.2 mm to the right, because doing so would require more than 10 mm of calibrated shadow data.

4.4.1 Data Fitting

Our end goal is to arrive at TCNR values as a function of the relative lateral positions of the SC and RoD and of the axial dimension of the SC. It is not very useful to use a discrete set of threshold values, especially since the produced data sets seem easy to interpolate. We thus begin by fitting the plots present in Figures 10 and 12.

Figure 10 and Figure 12 appear to be well-modelled by linear fits. I propose piecewise linear regressions for the 4 data sets present in these two figures. We define x_{lat} as the relative lateral displacement between the SC and RoD in mm. We define x_{ax} as the axial dimension of the SC in mm. Units are omitted in the table. Table 6 includes piecewise linear fits for data presented in Figure 10, and Table 7 includes piecewise linear fits for data presented in Figure 12. The minimal r^2 correlation coefficient value among the two segments in each piecewise fit is recorded.

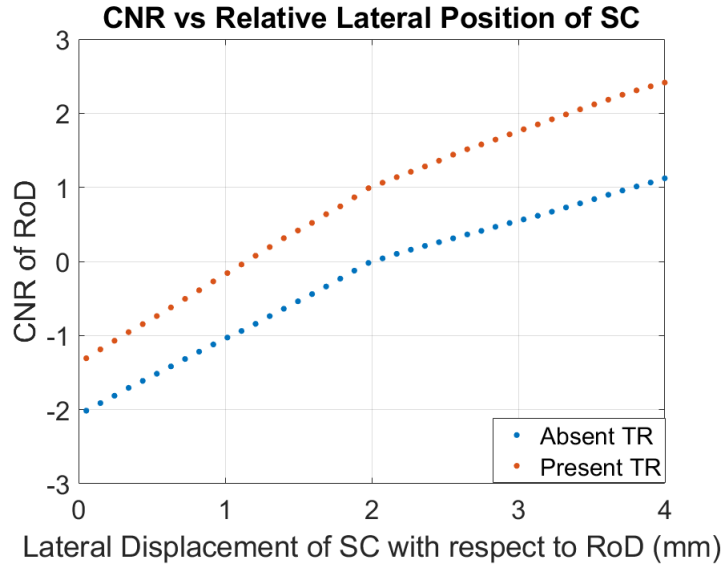


Figure 10: The variation of the CNR of the RoD with the lateral position of the SC relative to that of the RoD is displayed when the TR is absent (Blue) and present (Brown.) The upper axial bound of the SC is held constant at 4mm.

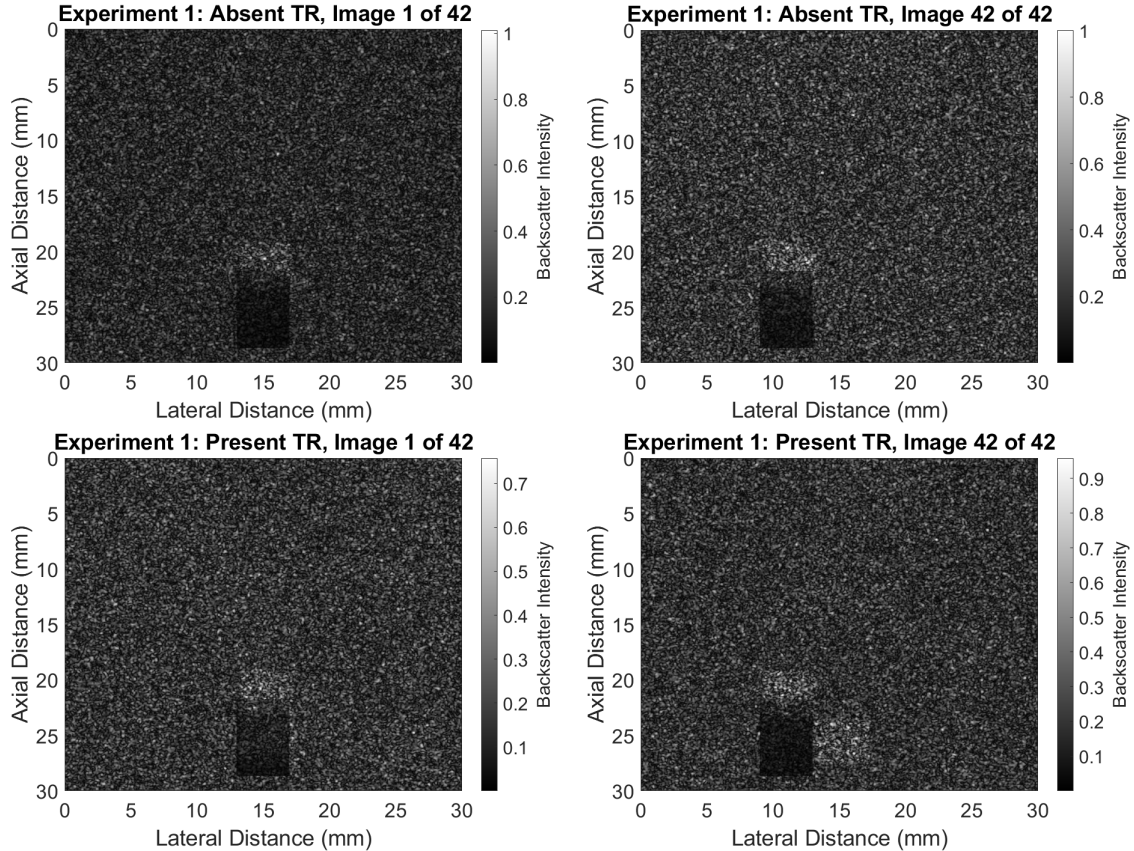


Figure 11: Four images corresponding to data points in Figure 10 are shown.

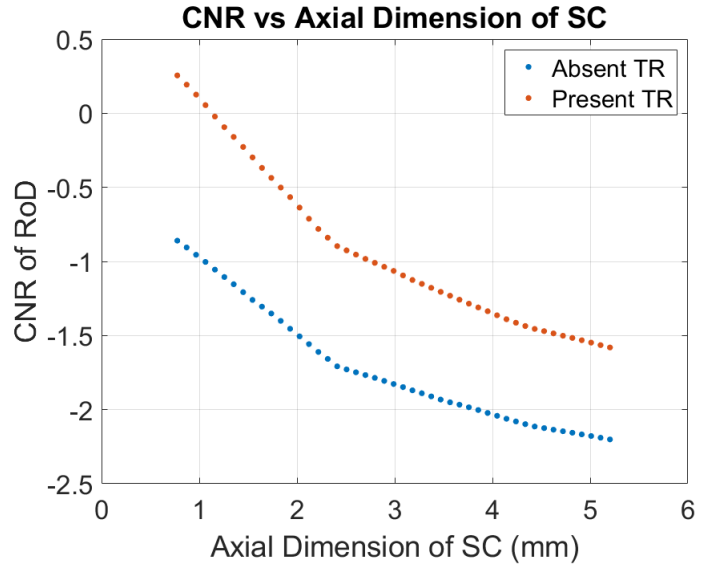


Figure 12: The variation of the CNR of the RoD with the axial dimension of the SC is displayed when the TR is absent (Blue) and present (Brown). The measured CNR is greatest when the SC has small axial dimension.

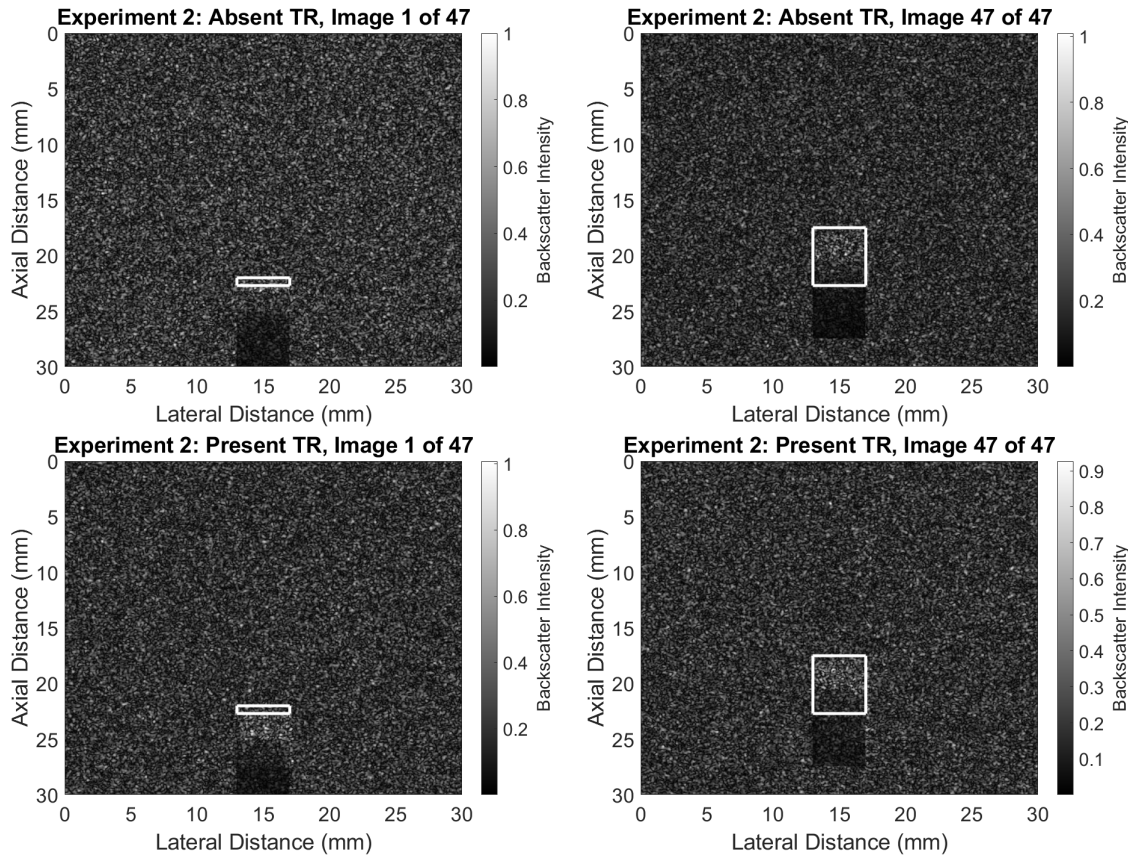


Figure 13: Four images corresponding to data points in Figure 12 are shown. The SC is outlined in white to emphasize the fact that the axial dimension of the SC is not constant.

The CNR plots in two dimensions have many (more than the 4 that would be expected by simply combining Tables 6 and 7 mathematically) roughly planar regions, and I do not consider it useful to define all of these regions in a piecewise manner.

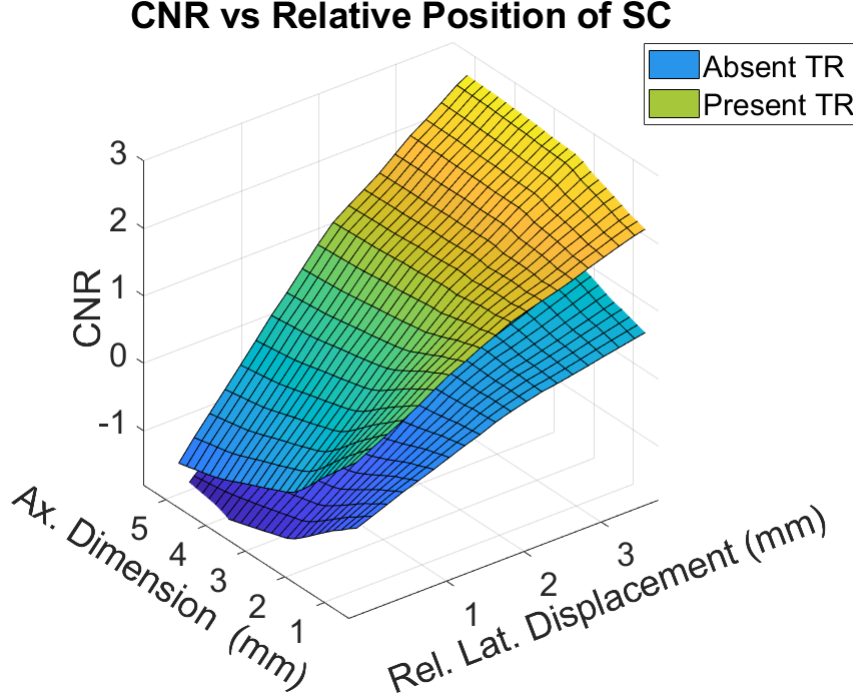


Figure 14: The variation of the CNR of the RoD with the relative lateral location and axial dimension of the SC is displayed when the TR is absent (Blue) and present (Green.) The patterns measured in experiments 1 and 2 persist, with one major exception - when the SC is laterally displaced far from the RoD, the CNR increases with Relative Axial Distance.

	CNR vs x_{lat}	r^2
Figure 10: Absent TR	$\text{CNR}(x_{lat}) = \begin{cases} 1.01x_{lat} - 2.04 & \text{if } x_{lat} < 1.98 \\ 0.56x_{lat} - 1.12 & \text{if } 1.98 < x_{lat} < 4 \end{cases}$	0.998
Figure 10: Present TR	$\text{CNR}(x_{lat}) = \begin{cases} 1.17x_{lat} - 1.33 & \text{if } x_{lat} \leq 1.98 \\ 0.71x_{lat} - 0.39 & \text{if } 1.98 < x_{lat} < 4 \end{cases}$	0.998

Table 6: Piecewise linear fit with regression coefficients for Figure 10. x_{lat} is measured in mm

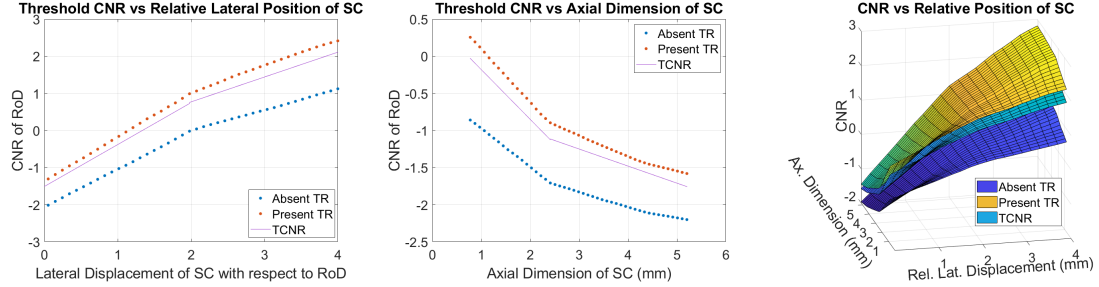


Figure 15: Threshold CNRs determined by Tables 6 and 7 as well as empirically calculated from Figure 14. The 3-dimensional image has been rotated to better show the TCNR surface.

	CNR vs x_{ax}	r^2
Figure 12: Absent TR	$\text{CNR}(x_{ax}) = \begin{cases} -0.52x_{ax} - 0.454 & \text{if } x_{ax} < 2.41 \\ -0.18x_{ax} - 1.29 & \text{if } 2.41 < x_{ax} < 5.21 \end{cases}$	0.990
Figure 12: Present TR	$\text{CNR}(x_{ax}) = \begin{cases} -0.72x_{ax} + 0.81 & \text{if } x_{ax} < 2.41 \\ -0.25x_{ax} - 0.32 & \text{if } 2.41 < x_{ax} < 5.21 \end{cases}$	0.990

Table 7: Piecewise linear fit with regression coefficients for Figure 12. x_{ax} is measured in mm.

4.4.2 Thresholds

If we use the fits derived in the ‘‘Present TR’’ portions of Tables 6 and 7 as our threshold values, we will fail to detect MCF-7 regions that happen to be appear slightly less bright on b-mode images than our simulated data. Likewise, if we use the fits derived in the ‘‘Absent TR’’ portions of Tables 6 and 7 as our thresholds, we will flag every shadowed region as hosting MCF-7 tissue.

For experiments 1 and 2, I define the Threshold CNR (TCNR) to be a 1:3 weighted mean of the Absent TR and Present TR piecewise fits present in Tables 6 and 7 respectively. For the first two experiments, I consider RoDs with a CNR value more than 3 times closer to the ‘‘Present TR’’ data set than the ‘‘Absent TR’’ data set. For experiment 3, no analytical fit was determined - I define the TCNR in this case as a 1:3 weighted mean of the ‘‘Absent TR’’ and ‘‘Present TR’’ surfaces in Figure 14.

The TCNR for experiment 1 is computed to be

$$TCNR(x_{lat}) = \begin{cases} 1.13x_{lat} - 1.51 & \text{if } x_{lat} < 1.98 \\ 0.67x_{lat} - 0.57 & \text{if } 1.98 < x_{lat} < 4 \end{cases}$$

The TCNR for experiment 2 is computed to be

$$TCNR(x_{ax}) = \begin{cases} -67x_{ax} + 0.49 & \text{if } x_{ax} < 2.41 \\ -0.23x_{ax} - 0.56 & \text{if } 2.41 < x_{ax} < 5.21 \end{cases}$$

Figure 15 shows plots present in Figures 10, 12, and 14 with threshold lines drawn in.

5 Discussion

The results from the wet lab section of the study offer values of enveloped radiofrequency data as produced by healthy tissue and MCF-7 tissue. This data informed the larger dry lab study, which offers threshold CNR values for the detection of MCF-7 tissue in acoustic shadows. If CNR values above these observed values are detected in a region of acoustic shadow, it is likely that the region hosts MCF-7 tissue. As expected, when more shadowing is present or when the shadow directly obscures the RoD, CNR values are the lowest. The 2-dimensional dependence of TCNR on the dimensions of the SC and the relative lateral position of the SC and RoD has the potential to be used to search a large 2-dimensional region of acoustic shadows for MCF-7 tissue.

The results from this study indicate that the TCNR values to be used for detection of MCF-7 tissue in acoustic shadows are strongly linear in both the relative displacement of the SC and the TR and the axial dimension of the SC, as linear fits relating these variables had strong correlation coefficients.

The results from Experiment 2 have the potential to be used by a clinician trying to determine the true (axial) size of a region of malignant tissue. The RoD and SC have the same lateral bounds, and save for a 0.3 mm axial gap can be considered to be parts of a cohesive MCF-7 tissue unit. This introduces a useful application. A clinician, in observing a single (not necessarily metastasizing) region of breast cancer tissue with attenuation similar to that of MCF-7 tissue, may be able to determine its axial dimension by computing the CNR of various regions inside the acoustic shadow cast by the same region. As an outline, they will model the single region to be composed of an SC region of unknown axial dimension combined with a posterior TR region (with unknown axial position). Then, they will iteratively compute the CNR for increasingly axially distant regions of tissue, until the CNR drops under the corresponding TCNR value. At this point, the MCF-7 tissue will be considered to end.

Due to the limited nature of calibration data, I was only able to calibrate the acoustic shadowing effect when the TR was directly beneath the SC. However, it is expected that the 0.3 dB/cm/MHz attenuation that might occur if larger regions of healthy tissue separate the SC from the RoD will not significantly impact results. Similarly, the usage of squares for tissue regions in place of more complicated and accurate scatterer geometries is not expected to impact results [16].

If highly experimental uses of ultrasound to treat breast cancer become mainstream methods of cancer treatment [5], the techniques discussed here have the potential to locate particularly harmful regions of metastasizing breast cancer tissue. This would allow ultrasound to be used as an all purpose tool to locate (using Ultrasound Imaging as in this paper), identify [18], and treat [5] breast cancer.

There are many natural ways to refine the model used here. The calibration of the shadowing effect can be made more precise by including more subregions C_i . Calibration data corresponding to MCF-7 phantoms shadowing healthy tissue can be created in the wet lab to avoid extrapolating on the shadow's effects on healthy tissue. The bright regions present in the calibration image should

be further investigated.

This paper explored only the highly specific case where MCF-7 tissue shadowed other MCF-7 tissue in a specific setting, but sets the precedent for many more potential studies. The relationship between the parameters of the transducer and TCNR values can be explored. The work can be tested in a clinical setting, using formalizations of the outlines for clinical use presented in this paper. The effects of other highly shadowing breast cancer lines can be calibrated, with similar computational experiments run, and resultant TCNR thresholds can be compared. The techniques used in this paper can be adapted for use with non-breast cancers. More generally, techniques discussed in this paper can be used with other imaging systems for which acoustic shadowing is a major concern.

6 Acknowledgements

I'd like to thank Dr. Jonathan Bennett for teaching me through NCSSM's Research in Physics program and Mr. Ben Levy for introducing me to the Field II software that I used for my simulations as well as for conducting the Calibration Experiment with parameters I specified.

References

- [1] BIERIG, S. M., AND JONES, A. M. Accuracy and cost comparison of ultrasound versus alternative imaging modalities, including ct, mr, pet, and angiography. *Journal of Diagnostic Medical Sonography* 25 (2009), 138 – 144.
- [2] BUSHNELL G. G., HONG, X. H. R. M., ET AL. High frequency spectral ultrasound imaging to detect metastasis in implanted biomaterial scaffolds. *Annals of biomedical engineering* 48 1 (1978), 477–89.
- [3] CHEUNG, K. J., PADMANABAN, V., SILVESTRI, V. L., SCHIPPER, K., COHEN, J. D., FAIRCHILD, A. N., GORIN, M. A., VERDONE, J. E., PIENTA, K. J., BADER, J. S., AND EWALD, A. J. Polyclonal breast cancer metastases arise from collective dissemination of keratin 14-expressing tumor cell clusters. *Proceedings of the National Academy of Sciences* 113 (2016), E854 – E863.
- [4] JENSEN, J. A., AND DE MUNK, P. J. Computer phantoms for simulating ultrasound b-mode and cfm images.
- [5] KENNEDY, J. E. High-intensity focused ultrasound in the treatment of solid tumours. *Nature Reviews Cancer* 5 (2005), 321–327.
- [6] LOTE, K., WALLØE, A., AND BJERSAND, A. J. Bone metastasis. prognosis, diagnosis and treatment. *Acta radiologica. Oncology* 25 4-6 (1986), 227–32.
- [7] MADSEN, E. L., ZAGZEBSKI, J. A., BANJAVIE, R. A., AND JUTILA, R. E. Tissue mimicking materials for ultrasound phantoms. *Medical physics* 5 5 (1978), 391–4.
- [8] NIGHTINGALE, K. R., CHURCH, C. C., HARRIS, G. R., WEAR, K. A., BAILEY, M. R., CARSON, P. L., JIANG, H., SANDSTROM, K., SZABO, T. L., AND ZISKIN, M. C. Conditionally increased acoustic pressures in nonfetal diagnostic ultrasound examinations without contrast agents: A preliminary assessment. *Journal of Ultrasound in Medicine* 34 (2015).
- [9] PATTERSON, M. S., AND FOSTER, F. S. The improvement and quantitative assessment of b-mode images produced by an annular array/cone hybrid. *Ultrasonic imaging* 5 3 (1983), 195–213.
- [10] PHAM, A. H., LUNDGREN, B., STAGE, B., PEDERSEN, M. M., NIELSEN, M. B., HEMMSEN, M. C., AND JENSEN, J. A. Shadow effects in simulated ultrasound images derived from computed tomography images using a focused beam tracing model. *The Journal of the Acoustical Society of America* 132 1 (2012), 487–97.
- [11] RODRIGUEZ-MOLARES, A., HOEL RINDAL, O. M., D’HOOGE, J., MÅSØY, S.-E., AUSTENG, A., AND TORP, H. The generalized contrast-to-noise ratio. In *2018 IEEE International Ultrasonics Symposium (IUS)* (2018), pp. 1–4.

- [12] SEYFRIED, T. N., AND HUYSENTRUYT, L. C. On the origin of cancer metastasis. *Critical reviews in oncogenesis* 18 1-2 (2013), 43–73.
- [13] SHARMA, G. N., DAVE, R. H., SANADYA, J., SHARMA, P., AND SHARMA, K. K. Various types and management of breast cancer: An overview. *Journal of Advanced Pharmaceutical Technology & Research* 1 (2010), 109 – 126.
- [14] SMITH, ET AL. *FREQUENCY INDEPENDENT ULTRASOUND CONTRAST-DETAIL ANALYSIS*. Pergamon Press, 1984.
- [15] STROHM, E. M., AND KOLIOS, M. C. Measuring the mechanical properties of cells using acoustic microscopy. *2009 Annual International Conference of the IEEE Engineering in Medicine and Biology Society* (2009), 6042–6045.
- [16] SZABO, T. Diagnostic ultrasound imaging: Inside out. Oxford Academic Press, 2014, ch. 1-4, pp. 1–116.
- [17] ZHANG, E., YANG, Z., SEILER, S. J., CHEN, M., LU, W., AND GU, X. Breast ultrasound computer-aided diagnosis using structure-aware triplet path networks. *ArXiv abs/1908.09825* (2019).
- [18] ZHI, H., OU, B., LUO, B., FENG, X., LING WEN, Y., AND YUN YANG, H. Comparison of ultrasound elastography, mammography, and sonography in the diagnosis of solid breast lesions. *Journal of Ultrasound in Medicine* 26 (2007).